A Refined Model for the Solution Structure of Oxidized Putidaredoxin[†,‡]

Thomas C. Pochapsky,*[,§] Nitin U. Jain,[§] Miklos Kuti,[§] Teresa A. Lyons,[||] and Jennifer Heymont[||]

Departments of Chemistry and Biology, Brandeis University, Waltham, Massachusetts 02254-9110

Received December 23, 1998; Revised Manuscript Received February 19, 1999

ABSTRACT: A refined model for the solution structure of oxidized putidaredoxin (Pdx^o), a $Cys_4Fe_2S_2$ ferredoxin, has been determined. A previous structure (Pochapsky et al. (1994) *Biochemistry 33*, 6424−6432; PDB entry 1PUT) was calculated using the results of homonuclear two-dimensional NMR experiments. New data has made it possible to calculate a refinement of the original Pdx^o solution structure. First, essentially complete assignments for diamagnetic ^{15}N and ^{13}C resonances of Pdx^o have been made using multidimensional NMR methods, and ^{15}N- and ^{13}C-resolved NOESY experiments have permitted the identification of many new NOE restraints for structural calculations. Stereospecific assignments for leucine and valine CH_3 resonances were made using biosynthetically directed fractional ^{13}C labeling, improving the precision of NOE restraints involving these residues. Backbone dihedral angle restraints have been obtained using a combination of two-dimensional J-modulated $^{15}N,^1H$ HSQC and 3D (HN)-CO(CO)NH experiments. Second, the solution structure of a diamagnetic form of Pdx, that of the C85S variant of gallium putidaredoxin, in which a nonligand Cys is replaced by Ser, has been determined (Pochapsky et al. (1998) *J. Biomol. NMR 12*, 407−415), providing information concerning structural features not observable in the native ferredoxin due to paramagnetism. Third, a crystal structure of a closely related ferredoxin, bovine adrenodoxin, has been published (Müller et al. (1998) *Structure 6*, 269−280). This structure has been used to model the metal binding site structure in Pdx. A family of fourteen structures is presented that exhibits an rmsd of 0.51 Å for backbone heavy atoms and 0.83 Å for all heavy atoms. Exclusion of the modeled metal binding loop region reduces overall the rmsd to 0.30 Å for backbone atoms and 0.71 Å for all heavy atoms.

The $Cys_4Fe_2S_2$ ferredoxin putidaredoxin (Pdx), the physiological reductant and effector for cytochrome $P450_{cam}$ (CYP101[1]), is the archetype for the class of ferredoxins that transfers electrons to type II cytochromes P450. The spectroscopic, biophysical, and physiological properties of Pdx have been a subject of active investigation for over thirty years (*1*−*4*). However, only within the past few years have structures begun to be published for this class of ferredoxin, which includes mammalian ferredoxins (adrenodoxin, renoredoxin) as well as bacterial ferredoxins such as terpredoxin, linredoxin, and megaredoxin. In 1994, we published a model for the solution structure of oxidized Pdx (Pdx^o), the first structure in this class of protein to be determined by any method (*5*) (PDB entry 1PUT). This structure was calculated using 878 NOEs, 66 dihedral angle restraints, and several paramagnetic broadening restraints that loosely positioned several structural features relative to the metal cluster binding region. The Pdx^o structure was classified as a model because the paramagnetism of the iron−sulfur cluster broadens ^1H resonances sufficiently to prevent the determination of high-resolution structural data (i.e., NOEs and J couplings) by standard NMR methods within ∼8 Å of the cluster (*6*). Because of the lack of a crystal structure for Pdx or for any closely homologous protein at that time, it was necessary to model the metal binding region of Pdx using the crystal structure of *Anabaena* ferredoxin (*7*), which has low (<10%) sequence homology with Pdx.

Recently, a considerable amount of new information has become available concerning the structure of the metal binding sites of Pdx and related ferredoxins. These data come from several sources. First, we have prepared a diamagnetic derivative of Pdx, permitting direct observation of residues near the metal binding site by high-resolution NMR methods. The reconstitution of Pdx with Ga^{3+} yields a colorless diamagnetic protein (GaPdx) containing a single gallium atom in which the major structural features of the native protein are conserved (*8*). We have described features of the metal binding site of GaPdx (*9*) and have determined the solution structure of the C85S variant of GaPdx, in which a serine replaces a nonligand cysteine in the Pdx sequence (*10*). Second, the crystal structure of a truncated bovine adrenodoxin (Adx) has been determined to 1.8 Å resolution, providing valuable information regarding the detailed struc-

[†] This work was supported by a grant from the National Institutes of Health (GM44191, T.C.P.).

[‡] Structures have been deposited with the Brookhaven PDB database (1PDX).

* Corresponding author. E-mail: pochapsky@binah.cc.brandeis.edu. Website: http://pochapsky.chem.brandeis.edu.

[§] Department of Chemistry.

[||] Department of Biology.

[1] Abbreviations: Adx, adrenodoxin; NMR, nuclear magnetic resonance; NOE, nuclear Overhauser effect; CT, constant time; CYP101, cytochrome $P450_{cam}$; NOESY, NOE spectroscopy; GaPdx, gallium-reconstituted putidaredoxin; HSQC, heteronuclear single quantum correlation; TOCSY, total correlation spectroscopy; TPPI, time proportional phase incrementation; Pdx^o, oxidized putidaredoxin; Tdx, terpredoxin; TSP, trimethylsilylpropionic acid sodium salt; 2D, two-dimensional; 3D, three-dimensional.

10.1021/bi983030b CCC: $18.00
Published on Web 03/26/1999

ture of the metal binding site for this class of ferredoxin (*11*). These data, plus a large number of new NOE restraints on the diamagnetic regions of Pdx^o obtained from ^{13}C- and ^{15}N-resolved NOESY experiments, have been used to calculate a refined model for the solution structure of Pdx^o.

MATERIALS AND METHODS

NMR Spectroscopy

Samples of uniformly ^{13}C,^{15}N-labeled Pdx were prepared for NMR experiments as described previously (*9*, *12*). A sample of Pdx with stereospecific ^{13}C labeling of valine and leucine methyl groups was prepared as described previously (*10*, *13*). Samples were typically 1−2 mM in 90/10 H_2O−D_2O with 10 mM d-Tris, pH 7.4, for NMR experiments.

All experiments were performed at 290 K on a Bruker AMX-500 spectrometer equipped with a three-channel Acustar pulsed field gradient amplifier and *x*, *y*, *z*-gradient triple resonance inverse detection probehead. The AMX-500 operates at 500.13, 50.68, and 125.76 MHz for ^{1}H, ^{15}N, and ^{13}C, respectively. ^{1}H chemical shifts are referenced to external DSS using the water signal as internal reference. ^{15}N chemical shifts are referenced to external liquid ammonia using the ^{1}H resonance of H_2O, and ^{13}C chemical shifts are reported relative to the methyl resonance of external TSP (*14*). Quadrature detection in indirect dimensions was achieved for all experiments using either hypercomplex or time proportional phase incrementation (TPPI) data acquisition. Either GARP-1 (*15*) or WALTZ-16 (*16*) composite pulse decoupling scheme was used for broadband decoupling of heteronuclei during acquisition. Data processing and analysis was performed using the Felix 97.0 software package operating on a Silicon Graphics O2 work station.

The NMR experiments used for sequential ^{13}C assignments of Pdx^o are essentially the same as those recently described for assignments in GaPdx (*9*). The HNCA experiment (*17*) was used for $^{13}C_\alpha$ assignments, while the HNCO experiment was used for assignment of carbonyl carbons (*18*). Complex data points were collected in the ^{1}H, ^{15}N, and ^{13}C dimensions, respectively: 512 × 22 × 32 (HNCA) and 512 × 32 × 32 (HNCO). Off-resonance decoupling of the $^{13}C'$ resonances in HNCA and of the $^{13}C_\alpha$ resonances in HNCO was achieved by a square pulse. For the HNCO experiment the ^{13}C carrier frequency was set in the middle of the carbonyl region at 125.7814311 MHz with a ^{13}C spectral width of 2600 Hz. For the HNCA experiment the ^{13}C carrier was placed in the middle of the alpha region at 125.766 692 8 MHz with a ^{13}C spectral width of 3250 Hz.

For side chain ^{13}C assignments CT-^{13}C HSQC (*19*) and HCCH-TOCSY (*20*) experiments were performed. For both experiments the ^{13}C carrier was placed in the middle of the aliphatic region at 125.764 203 9 MHz using a 8250 Hz spectral width. Two constant time HSQC experiments were recorded with 29.4 and 58.8 ms constant time delays. Complex data points (250) were collected in the indirectly detected dimension for the first experiment and 400 were collected for the second using States-TPPI for quadrature detection. ^{15}N decoupling during ^{13}C evolution was achieved using WALTZ-16 (*16*). The $^1/_4J_{CH}$ delay was set to 1.65 ms. Data processing involved convolution difference and multiplication with a Gaussian function in the directly detected dimension and linear prediction of 10% additional points and multiplication with an 80° shifted squared sine bell function in the indirectly detected dimension. The HCCH-TOCSY experiment was recorded using DIPSI-3 isotropic mixing (*21*) with a 21 ms mixing time. Data points [512 (complex) × 100 × 50] were collected in the two ^{1}H and ^{13}C dimensions, respectively. Quadrature detection was accomplished using TPPI. Data treatment was similar to the processing of the CT-HSQC experiments.

To obtain stereospecific methyl assignments for valine and leucine, we performed ^{1}H,^{13}C-HSQC experiments at 298 and 290 K with WATERGATE-type water suppression (*22*, *23*) and without ^{13}C decoupling during acquisition using a fractionally ^{13}C-labeled sample of Pdx prepared as described previously (*10*). These experiments exhibit splittings in the ^{13}C dimension which identify couplings between neighboring ^{13}C-labeled carbons, enabling stereospecific assignments of valine γ- and leucine δ-CH_3 resonances (*13*, *24*). For these high-resolution nonconstant time experiments, 1024 complex points were collected during t_2 for each of 2048 values of t_1. Quadrature detection in the t_1 dimension was obtained using TPPI. Spectral widths of 8440 Hz (^{13}C, t_1) and 6024 Hz (^{1}H, t_2) were used.

A combination of short (35 ms) mixing time TOCSY-^{1}H,^{15}N HSQC, and HNHB data obtained with uniformly ^{15}N-labeled samples were used to make stereospecific assignments of β-methylene protons and to assign χ_1 dihedral angles (*25*). These datasets were acquired with 512 (complex) × 54 × 128 and 512 (complex) × 64 × 128 data points, respectively, in t_3 (^{1}H observe), t_2 (^{15}N), and t_1 (^{1}H) dimensions. FIDs were processed with a 50 Hz convolution difference and a cosine bell function applied to all data points. Both indirect detect dimensions were multiplied by a 60° shifted sine bell function prior to Fourier transformation.

Estimates of backbone ϕ dihedral angles were made using either a $^3J_{HaHN}$-modulated ^{1}H,^{15}N HSQC experiment (*26*), which allows estimation of $^3J_{HaHN}$, or by measurement of $^3J_{C'C'}$ carbonyl couplings via an (HN)CO(CO)NH experiment (*27*). The $^3J_{HaHN}$-modulated ^{1}H,^{15}N HSQC experiment was performed with standard ^{1}H,^{15}N HSQC parameters using a series of 10 coupling evolution times ranging from 20 to 120 ms. The (HN)CO(CO)NH experiment was performed with the ^{15}N carrier frequency set to 120 ppm. The ^{13}C frequency was set in the carbonyl region (177.2 ppm), and low-power on- and off-resonance square pulses were used to selectively excite ^{13}C resonances in the carbonyl and C_α regions, respectively. Complex points [58 (t_1 ^{13}C) × 45 (t_2 ^{15}N) × 512 (t_3 ^{1}H)] were collected with acquisition times of 27 ms (t_1 ^{13}C), 27 ms (t_2 ^{15}N), and 85 ms (t_3 ^{1}H). Isotropic mixing of the ^{13}C carbonyl resonances was accomplished using a DIPSI-3 sequence (*21*), with an isotropic mixing period of 115 ms. Water suppression was achieved using the WATERGATE sequence (*23*). Quadrature detection in the t_1 and t_2 dimensions was accomplished using the States-TPPI method. Thirty-two fids were collected for each increment, resulting in an experimental duration of 4 days. The fids were 50% truncated and apodized with a squared cosine bell in the t_3 dimension. In the t_2 and t_1 dimensions the data was extended by linear prediction to 60 and 80 points, respectively, and apodized with a 70° shifted sine bell. The resulting data matrix contains 128 (ω_1) × 128 (ω_2)

$\times$ 512 (ω_3) points, with spectral widths of 2200 Hz (ω_1 ^{13}C) $\times$ 1700 Hz (ω_2 ^{15}N) $\times$ 6048 Hz (ω_3 ^{1}H).

Structural Calculations

New NOE restraints for structural calculations were obtained from 3D ^{13}C- and ^{15}N-edited NOESY spectra obtained at 500 MHz. A mixing time of 70 ms was used for all NOESY experiments, since examination of NOE buildup curves indicated that NOE cross-peaks obtained at this mixing time are essentially free of spin diffusion effects (*5*). Strong NOEs were assigned distances of $\leq$3 Å, medium NOEs $\leq$4 Å, and weak NOEs $\leq$5 Å, with an allowed error of +0.3 Å without energy penalty. Close approach to the sums of their van der Waals radii was permitted for all NOE restraint pairs without penalty. ϕ dihedral angle restraints were obtained from NH$-$C$_\alpha$H coupling constants as obtained from J-modulated ^{1}H,^{15}N HSQC experiments or from backbone C′-C′ carbonyl carbon couplings as measured using the (HN)CO(CO)NH experiment. In cases where good agreement ($\leq$10°) was obtained for a ϕ dihedral angle from both methods, an angular variation of $\pm$20° was permitted from the assigned dihedral angle without energetic penalty. If data from only one experiment was available or the results from one or the other were ambiguous, a variation of $\pm$40° was permitted without energetic penalty. Although in no case did the data from the two experiments contradict each other, the carbonyl coupling data generally gave less ambiguous results. As neither experiment distinguishes between positive and negative values of ϕ, it was necessary to test both values for several residues in order to determine which best fit the observed data (vide infra).

Structural calculations were performed on a Silicon Graphics O2 work station running XPLOR 3.851 (A. Brunger, Yale University). A modification of the combined distance geometry-simulated annealing protocol of Nilges et al. was used for the calculations (*28*). The structure of the Fe_2S_2 cluster (Fe$-$S bond lengths and angles) was defined from crystal structures of model compounds (*5*, *29*). A first round of distance geometry calculations was performed as follows. One of the family of published solution structures of Pdx was used as a template for pseudoatom corrections and for configurational constraints. A set of substructures was then generated using distance geometry (bound smoothing, substructure embedding, and regularization). Substructures were tested for the correct enantiomer first by comparison of the energies due to violations of improper angles defining chirality around stereocenters in the protein with those generated by reflection of the substructure along the *x*-axis, and then by comparison of the substructure and its reflection with a reference structure generated from the published structure of Pdx^o. Those substructures which passed the test for the correct enantiomer were then subjected to simulated annealing for further refinement. The template structure was used to generate all atoms and local idealized geometries for the embedded substructures. The resulting structures were then energy-minimized with respect to bonds, van der Waals contacts, NOEs, and modeling constraints prior to simulated annealing. To account for remaining nonstereospecific assignments, NOEs to aromatic protons and to equivalent protons of methyl groups, we used r^{-6} averaging of NOE-defined distances in all structural calculations. High-temperature annealing (2000 K) was performed for 1000 steps (Δt = 3 fs), during which improper angles defining chirality and planarity of peptide bonds and aromatic rings were slowly introduced and van der Waals interactions increased. The structures were then cooled to a final temperature of 100 K over 1000 fs steps and minimized. Energies were determined using bond lengths, bond, dihedral, and improper angles, van der Waals contacts, NOEs, and modeling restraints. No electrostatic terms were used in calculating energies. The structures shown here were selected from a total of 400 structures calculated using the final restraint set, and exhibit no NOE violations greater than 0.5 Å and no dihedral angle violations greater than 5°.

RESULTS

^{13}C and Stereospecific ^{1}H Resonance Assignments

Because of the availability of essentially complete ^{1}H and ^{15}N assignments for the diamagnetic regions of Pdx^o (*6*, *12*), the sequential assignment of ^{13}C resonances of Pdx^o was straightforward. HNCA data provided both intra- and interresidue connectivities, verifying previous backbone ^{1}H and ^{15}N sequential assignments. HNCO data gave interresidue correlations from amide ^{15}N to carbonyl ^{13}C resonances. HCCH-TOCSY data was used to correlate side chain ^{1}H and ^{13}C resonances. In several cases, ambiguities regarding the correct assignments of ^{1}H resonances within long side chain spin systems such as lysine and arginine were resolved by ^{1}H,^{13}C HSQC data. Stereospecific assignments of C$_\beta$H$_2$ protons were made using a combination of HNHB and short mixing time TOCSY-HSQC data on ^{15}N-labeled samples (*25*).

By virtue of the large one-bond J-couplings involved in heteronuclear coherence transfer, some ^{1}H resonances near the paramagnetic region that could not be identified in our earlier homonuclear experiments (*6*), particularly those corresponding to resonances of Met 24, Gln 25, His 49, Met 70, Leu 71, and Gln 87, are now identified sequentially. However, considerable regions of Pdx^o are still inaccessible to sequence-specific resonance identification due to paramagnetic broadening. These include the complete spin systems of residues 36$-$48 and 84$-$86 and portions of the spin systems of Met 24, Gln 25, and His 49.

The use of biosynthetically directed fractional ^{13}C labeling of Val and Leu side chains permitted the stereospecific assignment of diastereotopic methyl groups in ^{1}H,^{13}C HSQC spectra obtained without refocusing of ^{13}C$-^{13}$C couplings in the ^{13}C dimension (*13*, *24*).

Experimental Restraints in the Diamagnetic Region of Pdx^o

As with our previous structural determination for Pdx^o, NOE and experimentally determined dihedral restraints for the current set of calculations are limited to diamagnetic regions of the protein. However, the availability of three-dimensional heteronuclear-edited NOE experiments has greatly increased the number of NOE restraints available for the current calculations. Our original structure was restrained by 878 NOEs. In the current calculations, a total of 1171 NOEs were used. Furthermore, the greatly increased number of stereospecifically assigned NOE restraints in the current set (particularly those to Val and Leu methyl groups) has

Table 1. Summary of Experimental and Modeling Restraints Used in Calculation of the Refined Model of Pdx

experimental restraints		modeling restraints	
NOEs (total 1171)		distance restraints from GaPdx (total 175)	
interresidue (short range, $i - j \leq 4$)	461	interresidue	148
(long range, $i - j > 4$)	437		
nontrivial intraresidue	273	nontrivial intraresidue	29
dihedral restraints (total 121)		dihedral restraints from GaPdx (total 16)	
ϕ	78	ϕ	11
χ_1	44	χ_1	5
hydrogen bonds in regular secondary structure	18	metal cluster binding site (from Adx structure)	
		distance between C_α carbons of ligand Cys	6
		angular restraints	
		ϕ (G37-C48)	11
		ψ (G37-C48)	11
		χ_1 (Cys 39,45,48,86)	4

improved the precision with which the structures are calculated.

Similarly, the use of three-dimensional heteronuclear experiments designed to measure three-bond coupling constants (J-resolved ^{1}H,^{15}N HSQC for measurement of $^3J_{HNHa}$, (HN)CO(CO)NH for measurement of $^3J_{C'C'}$) increases the number and improves the reliability of dihedral restraints used. Our previous structure calculations used 66 experimentally derived ϕ dihedral restraints. The current structures are calculated using 78 such restraints. Also, the use of HNHB and shortmixing time ^{1}H,^{15}N-TOCSY HSQC data has provided χ_1 angle estimates for 44 residues in the diamagnetic region of Pdx^o.

The restraint set for the diamagnetic regions of Pdx^o includes a set of 18 hydrogen bonds, all from regular secondary structural features in the diamagnetic region, that occur repeatedly in accepted structures calculated using the complete restraint set described in Table 1 excluding hydrogen bonding restraints. Inclusion of the hydrogen bonds does not change the results of the structure calculations other than to increase the rate at which acceptable structures are obtained in the course of the structure calculations.

Modeling of the Metal Binding Site and Environs

Restraints from the GaPdx Structure. GaPdx conserves the global fold of Pdx^o (*9*, *10*). With the exception of the C-terminal region of the polypeptide (Asp 103-Trp 106), which interacts more strongly with the rest of the structure in Pdx^o than in GaPdx, those structural features that can be directly compared between the two proteins by NMR are very similar (*10*). The solution structure of GaPdx offers a number of insights into the structural roles of residues that could not be determined in Pdx^o due to paramagnetism of the metal center, and we have used the GaPdx structure to aid in modeling the native Pdx structure near the metal binding site in Pdx^o. This has been accomplished using some NOEs identified in GaPdx as restraints in the current calculations.

Caution is required in deciding which structural features of GaPdx are expected to be present in the Pdx^o structure and which are not. We have restricted our use of GaPdx-derived structural restraints to NOEs that are observed in GaPdx between residues in the core region of the protein, that is, NOEs that do not involve residues in the metal binding loop (Gly 37-Cys 48) or the C-terminal residues Asp 103-Trp 106. Due to the nonisosteric nature of the metal replacement, it is expected that the metal binding loop will be distorted significantly in GaPdx relative to the native protein (vide infra), and as noted previously (*10*), the C-terminal residues in GaPdx are considerably less restrained in GaPdx than in the native protein.

Model Constraints on the Metal Binding Site from the Adx Crystal Structure. Considerable sequence, structural, and functional homology exists between Pdx and the family of mammalian ferredoxins that supply electrons to cytochromes P450 in steroid biosynthetic pathways. The crystal structure of one member of this class, a truncated form of oxidized bovine adrenodoxin (Adx 4-108), has recently been published (*11*). The Adx structure provides the first detailed picture of an unperturbed Fe_2S_2 binding site from this class of ferredoxin. Although sequence homology between Pdx and Adx is only about 35%, there is good homology in the metal binding loop (G37-D38-C39-G40-G41-S42-A43-S44-C45-A46-T47-C48-H49 for Pdx, G44-A45-C46-E47-G48-T49-L50-A51-C52-S53-T54-C55-H56 for Adx), and the structures of the two proteins are very similar (vide infra), with a 1.64 Å rms difference between the Adx structure and the average of the 1PUT family of 12 structures for Pdx^o (*11*). In particular, the positions of the Fe and S atoms of the metal clusters superimpose almost exactly in the two structures. This observation justifies (within limits) the homology modeling approach to building metal binding site structure into paramagnetic proteins, and implies that the Adx structure is a suitable guide for modeling the metal binding loop in the current refinement of the Pdx structure.

For the most part, modeling restraints obtained from the Adx structure take the form of backbone dihedral angle (ϕ and ψ) restraints on residues in the metal binding loop (G37-D38-C39-G40-G41-S42-A43-S44-C45-A46-T47-C48) and χ_1 restraints on the side chains of the cysteinyl ligands of the Fe_2S_2 cluster (Table 1). However, the C_α carbons of the four cysteinyl ligands (Cys 39, Cys 45, Cys 48, and Cys 86) and residues of Pdx^o were constrained loosely to a planar trapezoid defined by the experimental distances between the corresponding four atoms (the C_α carbons of Cys 46, Cys 52, Cys 55, and Cys 92) in the Adx crystal structure. As with our previous calculations, for which the *Anabaena* ferredoxin structure was used to model the Pdx binding site (*5*, *7*), this proved to be the most effective means to model the cluster with the least number of restraints.

Description of the Refined Pdx Structural Model

A family of 14 structures of Pdx^o are presented here (Figures 1 and 2). Statistics for the structures are shown in

FIGURE 1: Stereoview of the superimposed backbone traces of fourteen structures of Pdx^o generated as described in the text. Presentation is from approximately the same point of view as in Figure 2. Structures exhibit an overall backbone rmsd of 0.51 and 0.83 Å for all heavy atoms. Exclusion of residues 36−48 (metal binding loop) improves the rmsd to 0.30 Å (backbone) and 0.71 Å (all heavy atoms). The figure was generated using MOLMOL (ETH Zürich).

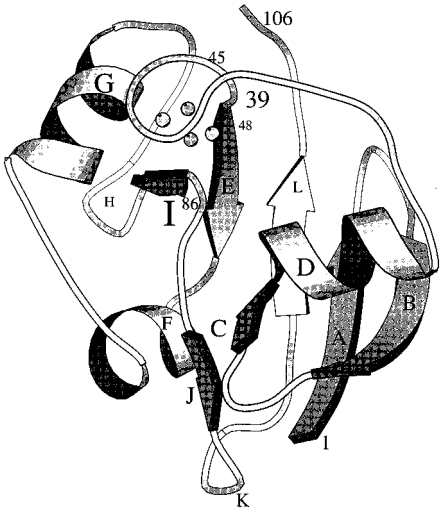

FIGURE 2: Secondary structural features of Pdx. The Fe−S cluster is represented by spheres in the top center of the figure: (A) Ser 1-Val 6, (B) Arg 12-Val 17, (C) Val 21-Ser 22, (D) Leu 23-Gly 31, (E) Val 50-Asn 53, (F) Ala 55-Pro 61, (G) Glu 65-Cys 73, (H) Lys 79-Ser 82, (I) Ser 82-Leu 84, (J) Ile 88-Met 90, (K) Thr 91-Leu 94, and (L) Ile 97-Pro 102. The figure was generated using MOLSCRIPT (*54*).

the caption of Figure 1. None of the structures presented exhibit any NOE violations greater than 0.5 Å or dihedral angle violations greater than 5°. In the diamagnetic region of the protein, all nonglycinyl residues exhibit ϕ and ψ angles for the polypeptide backbone in the allowed negative ϕ angle regions of $\phi-\psi$ space (see Figure 3). PROCHECK_NMR (*30*) reports that 58.8% of all nonglycinyl residues in the fourteen models are in the most favored regions of the Ramachandran plot, with 41.0% in the additional allowed regions; 0.2% are found in generously allowed regions and none are found in disallowed regions. Removal of the modeled region of the metal cluster binding loop (residues 36−48) changes the PROCHECK results only minimally, with 62% found in the most favored regions, 37.7% in the additional allowed regions, and 0.3% in the generously allowed regions. Of the nonglycinyl residues, only Ala 43 in the metal binding loop is found in the allowed positive ϕ angle region, since it is modeled from the corresponding residue in Adx, Leu 50 (*11*).

DISCUSSION

Validity of the Modeling

The previously published structure of Pdx (*5*), which is also a hybrid structure combining experimental data with modeling of the metal cluster environs, has been used successfully as a guide for mutagenesis studies in Pdx and Adx (*31*−*35*) as well as for a variety of homology modeling and theoretical studies (*4*, *36*−*40*). It was noted by the authors of the Adx crystallographic study (*11*) that in a best-fit superposition of the Pdx^o structure with the Adx structure, the crystallographically determined positions of the atoms in the Fe_2S_2 cluster in Adx superimpose almost precisely on the corresponding atoms as modeled in the Pdx^o structure (*5*). This observation confirms the validity of the homology method of generating structures for this type of ferredoxin. However, as in any case where experimental data is combined with modeling, the limits to which the resulting structure may be appropriately interpreted must be addressed. It must be clear which regions of the structure are defined only by experimental results and where modeling has been used to do this (see Figure 4). The caption of Figure 4 indicates by color coding and designation the types of restraints used in a particular region of the protein. Positions of residues in Pdx sufficiently far from the metal cluster so that no paramagnetic effects are apparent are defined solely from experimental data. As the metal cluster is approached (~10 Å), restraints derived from NOEs observed in the GaPdx structure are used in combination with the available experimental data. Finally, the restraints on the metal cluster binding loop and the cluster itself are determined solely on the basis of homology modeling from the Adx crystal structure.

The use of modeling restraints based on NOEs or J-couplings measured for GaPdx is limited only to those residues that are expected to occupy identical positions in native Pdx and GaPdx. Practically, this excludes the use of such restraints for all residues in the C-terminal peptide (Asp 103-Trp 106) or in the metal binding loop. The replacement of the Fe_2S_2 cluster in native Pdx with a single Ga^{3+} ion in GaPdx is not isosteric, and some distortion of the metal binding site is to be expected. However, there are reasons

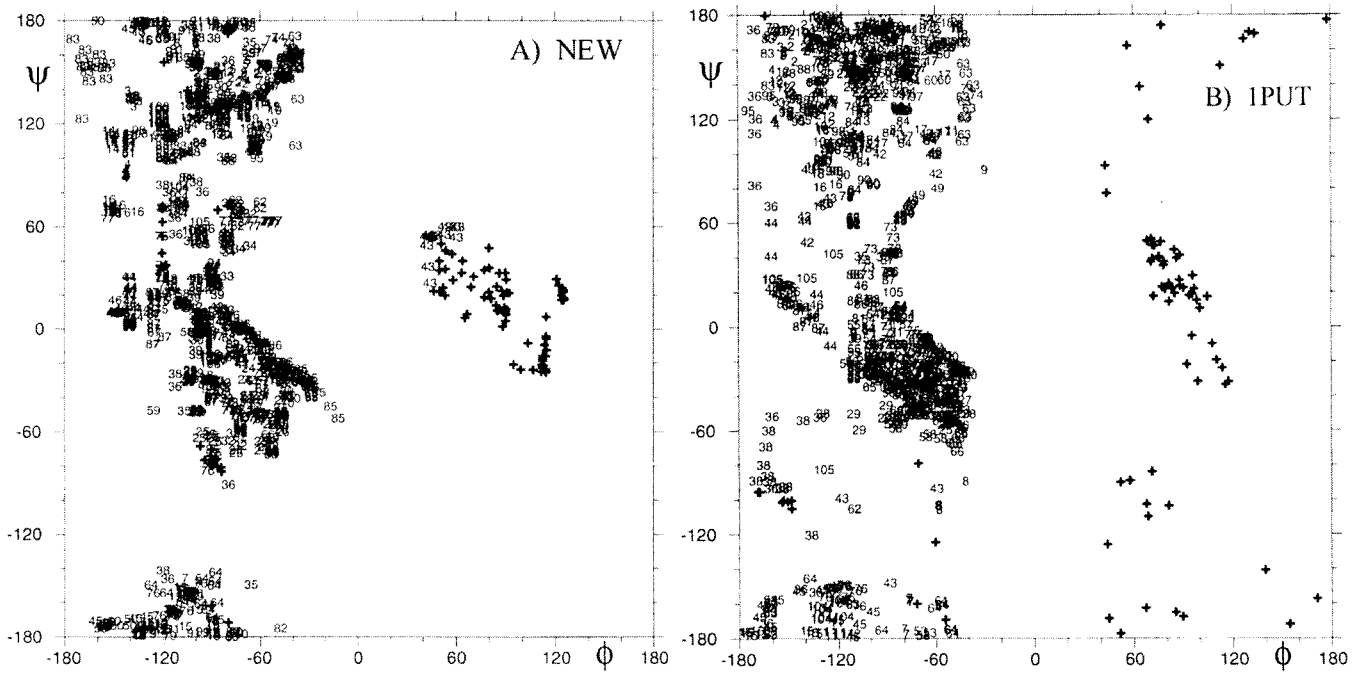

FIGURE 3: Ramachandran diagrams of (A) fourteen structures of Pdx^o generated in the current refinement and (B) a family of 12 structures (1PUT) (*5*). The figure was generated using MOLMOL (ETH Zürich). Glycine residues are represented by crosses, and all others are represented by residue number.

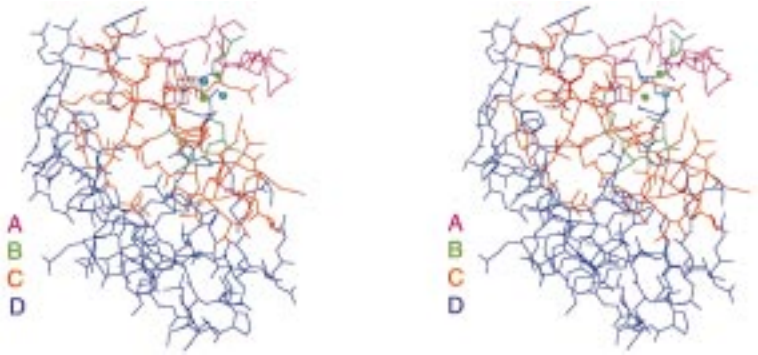

FIGURE 4: Stereoview of one of the current structures of Pdx^o color coded to indicate the structural distribution of the various types of restraints used in modeling the Fe_2S_2 cluster binding site and environs. For clarity, the structure is viewed from a perspective standing on the left-hand side of the structure (near helix **G**) as shown in Figures 1 and 2. The Fe_2S_2 cluster atoms (upper right) are shown as green spheres. The key to color-letter coding on lower left: (A) metal binding loop residues (Gly 37-Cys 48) modeled from Adx crystal structure only; (B) residues Val 36 and Leu 84-Cys 86 are modeled from GaPdx restraints only; (C) combination of experimental restraints (NOEs and J-coupling in Pdx^o) and restraints based on NOEs observed in GaPdx; and (D) only Pdx^o experimental restraints (residues 1−20, 30−31, 53−63, 75−77, 79−81, 90−100, and 102−106). The figure was generated using MOLMOL (ETH Zürich).

to expect that much of this distortion will be restricted to the flexible metal binding loop of polypeptide that contains three of the four cysteines ligating the metal cluster (G37-D38-C39-G40-G41-S42-A43-S44-C45-A46-T47-C48). Several considerations support this. First, there is evidence that small differences in the metal binding loop strongly affect the nature of metal binding. Unlike Pdx, *Anabaena* ferredoxin can be reconstituted with a complete Ga_2S_2 cluster (*41*), despite considerable similarity in the core structures of the proteins near the metal binding site. The metal binding loop of Pdx is one residue longer (C-G-G-S-A-S-C-A-T-C) and contains two more glycines than that of *Anabaena* ferredoxin (C-R-A-G-A-C-S-T-C), and so is likely to be more flexible than the *Anabena* loop and may be able to adjust to the steric requirements of binding a single metal ion (*10*). Second, preliminary free energy perturbation (FEP) calculations using the GIBBS (UCSF) program and AMBER force field, in which the single Ga^{3+} ion of GaPdx is replaced in the course of the simulation by an Fe_2S_2 cluster, suggest that conformational changes in the metal binding loop are the most significant responses of the polypeptide to the perturbation induced by the nonisosteric replacement; the structure of the rest of the protein is relatively unperturbed (Pochapsky, unpublished results). Finally, but most importantly, NMR data from GaPdx and Pdx^o also support this conclusion. The chemical shifts for resonances in the core of the protein where the GaPdx-derived restraints are used close to the metal cluster that could be assigned in Pdx^o are similar (except for those of the C-terminal residues (Asp 103-Trp 106)) to their counterparts in GaPdx, and the NOEs that are observed to those resonances from nearby residues in the diamagnetic region are the same in both native and GaPdx. As a final check, the crystal structure of Adx was used for comparison when appropriate to ensure that the GaPdx-derived restraints used in the current calculations are not unreasonable.

FIGURE 5: Stereoview of the superposition of the backbone atoms of the mean of the current family of Pdx^o structures (heavy lines) onto the backbone atoms of the mean structure of the older Pdx^o structures 1PUT (*5*), shown as a light line. rmsd for the two superimposed structures is 1.76 Å. Orientation is approximately the same as in Figures 1 and 2. Superpositions, mean structures, and the figure were generated using MOLMOL (ETH Zürich).

Comparison of the Current Family of Structures with 1PUT and with Adx

The most obvious differences between the 1PUT structures (*5*) and the current set of structures are the improved rmsd values of the new structures and a considerable improvement in the Ramachandran diagrams (Figure 3). Much of this improvement is no doubt due to the larger constraint set used for the calculations. It is also likely (although it cannot yet be confirmed) that the Adx structure is a more reliable template for modeling of the Pdx metal binding site than the *Anabaena* ferredoxin structure, simply due to the high degree of structural homology between Pdx and Adx in regions that can be directly compared.

The current family of structures corrects two deficiencies of the 1PUT structures. First, the aromatic ring of Tyr 33 is now partially inserted into the body of the structure, rather than being completely surface exposed as in the 1PUT structures. Second, the tilt of helix **G** relative to the rest of the structure is changed somewhat, and the large apparent mobility of the **G** helix in the 1PUT structures is greatly reduced. Both of these corrections result from the use of the restraint set obtained from GaPdx. In native Pdx, no nonsequential NOEs were observed to the aromatic ring protons of Tyr 33, so the Tyr 33 side chain was not constrained into the protein interior in the calculation of the 1PUT structures. However, in GaPdx NOEs are observed between the Tyr 33 ring protons and the $C_\alpha H$ of Cys 85 and with several side chain resonances of Met 24, all of which are affected by paramagnetic broadening in the native protein. Inclusion of these NOEs as modeling restraints in the current calculations results in a positioning of the Tyr 33 aromatic ring partially buried in the protein interior in a position analogous to that of an aromatic residue in Adx, Phe 43 (vide infra). Similarly, a set of NOEs were detected in GaPdx between the newly identified methyl protons of Leu 71 on the **G** helix to the aromatic ring of Tyr 51 and the CH_2 protons of Ser 82 in the C-terminal cluster. Lacking these restraints on the paramagnetically broadened resonances of Leu 71, the 1PUT structures do not place the Leu 71 side chain close to either Tyr 51 or Ser 82, resulting in a different tilt to helix **G** than is observed in this new set of structures. Furthermore, the apparent mobility of helix **G** in the 1PUT structures was an artifact of the lack of NOE restraints between the **G** helix and the rest of the protein. The use of the core NOEs observed in GaPdx as restraints in the current calculations greatly reduces the degree of mobility exhibited by the **G** helix. Figure 5 shows a superposition of the average structure from the new calculations superimposed on the average structure of 1PUT. The two structures show an rmsd of 1.76 Å, with much of the difference observed in helix **G** and residues 33−36.

The availability of the Adx crystal structure provides an independent check for both the accuracy of the experimental data used in the current structural calculations as well as the reasonableness of the modeling performed. Pdx and Adx show the same folding topology, with only minor differences in secondary structure. Sequence alignment of the Adx structure onto the current Pdx^o structure nearest the mean of the fourteen structures presented gives an rmsd of 1.77 Å (Figure 6). Furthermore, many of the specific features of Pdx discussed previously (*5*, *42*) have close counterparts in the Adx structure. For example, the interaction domain of Adx (*11*) is structurally similar to that part of Pdx we previously termed the C-terminal cluster, a small compact region consisting of side chains from residues His 49, Tyr 51, Val 74, Thr 75, Ala 76, Asp 77, Leu 78, Lys 79, Ser 82, and Arg 83 and the C-terminal residues Pro 102, Asp 103, Arg 104, Gln 105, and Trp 106 (*42*). For convenience, in the comparison with the Adx structure, we will for the current discussion also refer to the C-terminal cluster as the interaction domain of Pdx. The interaction domain, which in the latest structures also formally includes Asp 67, Met 70, and Leu 71, is located in the upper left-hand corner of the Pdx structure as shown in Figure 2. A more detailed view of the Pdx interaction domain is shown in Figure 7. As the name suggests, this domain has been implicated in redox partner recognition for both Adx and Pdx. The results of chemical modification and mutagenesis experiments demonstrate that acidic residues along the outside surface of the **G** helix in Pdx (Glu 65, Glu 72) may be important for the interaction with PdR (*34*, *43*). The C-terminal Trp 106, also part of the cluster, has long been identified as important for interaction with cytochrome $P450_{cam}$ (*44*, *45*). Although Adx shows a different set of regiospecificities for interaction with its cognate redox partners, evidence indicates that the same region of the protein is involved in binding redox partners (ref *11* and references therein).

In both Pdx and Adx, the interaction domain is held together by a combination of electrostatic, hydrogen bonding, and hydrophobic interactions. We have shown that protein dynamics in this region of Pdx are very sensitive to the metal cluster oxidation state (*12*). No redox-dependent measure-

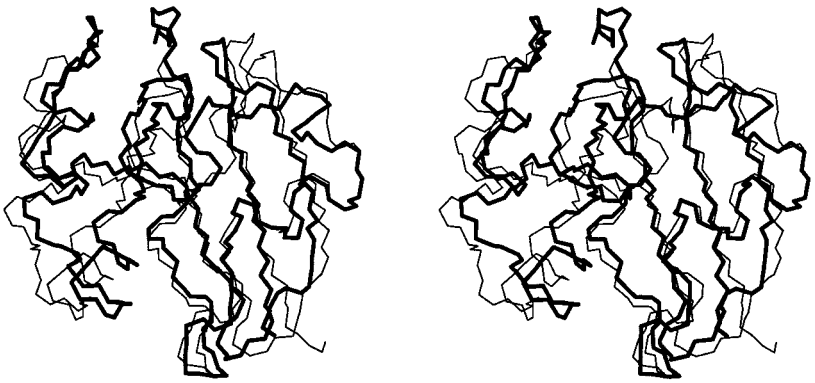

FIGURE 6: Stereoview of the superposition of the backbone atoms of one of the current family of Pdx° structures (heavy lines) onto the backbone atoms of crystallographic structure of bovine adrenodoxin (Adx), shown as a light line (*11*). rmsd for the two superimposed structures is 1.77 Å. Superposition and the figure were generated using MOLMOL (ETH Zürich).

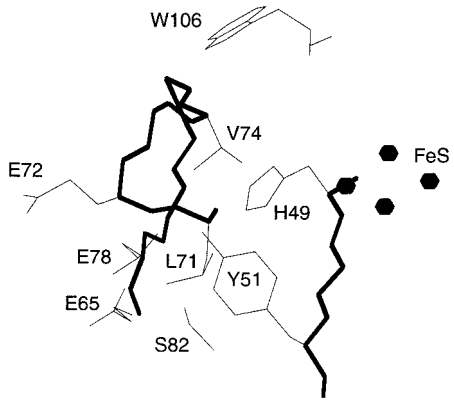

FIGURE 7: Details of the interaction domain (C-terminal cluster) in Pdx. NOE, slow OH and NH exchange, and chemical shift evidence suggest the involvement of His 49, Tyr 51, and Ser 82 in a strong hydrogen bonding network (Pochapsky et al., 1994). The Leu 71 side chain is in close contact with the Ser 82 and Tyr 51 side chains, and the Trp 106 indole ring exhibits NOEs to Val 74, as does the imidazole of His 49. The figure was generated using MOLMOL (ETH Zürich).

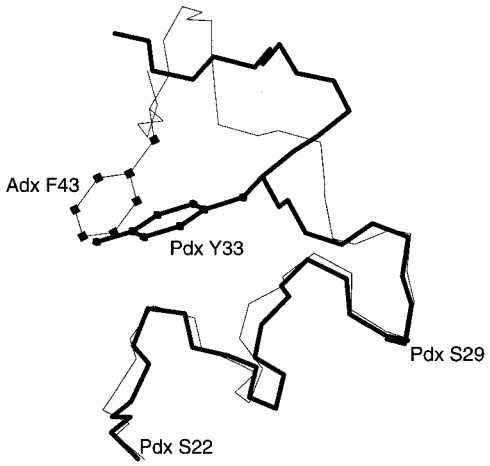

FIGURE 8: Positions of nonhomologous residues Phe 43 (Adx) and Tyr 33 (Pdx) structures superimposed as in Figure 5. Heavy lines indicate the backbone of Pdx. The backbone of Adx is shown as light lines. Similar positioning of the Phe 43 and Tyr 33 side chains in their respective structures results in differing backbone conformations between Pdx and Adx in this region. The figure was generated using MOLMOL (ETH Zürich).

ments of amide proton exchange rates in the interaction domain of Adx have been published, but amide exchange in the metal binding site of Adx is very sensitive to the oxidation state, as measured by ESEEM (*46*), and reduction does appear to have a significant effect on global amide exchange in human ferredoxin, which is nearly identical to bovine adrenodoxin in sequence (*47*). We have proposed that this dependence of the dynamics on redox state may be the result of changes in polar interactions in the C-terminal cluster resulting from changes in the oxidation state at the metal center (*48*). Alternatively, Müller has proposed that redox-dependent modulation of this region in Adx is the result of a mechanical linkage provided by the side chain of His 56 (His 49 in Pdx), which is immediately to the C-terminal side of the Fe−S ligand Cys 55 (Cys 48 in Pdx). The imidazole side chain of His 56 is hydrogen bonded to backbone and side chain positions in the interaction domain (*11*), and any redox-dependent changes in structure or dynamics of the metal binding site could be transmitted mechanically to the interaction domain via these hydrogen bonds. This hypothesis is supported by our recent observation that the redox dependence of protein dynamics as measured by amide proton exchange in terpredoxin (Tdx), another member of this class of ferredoxins, is much less than in Pdx. In Tdx, His 49 is replaced by an arginine, presumably weakening the mechanical linkage between the metal binding site and the interaction domain by replacing the stiffer histidine side chain with the more flexible arginine side chain (Mo and Pochapsky, unpublished results).

There are two differences between the Pdx and Adx structures that should be noted. As we described in our publication concerning the GaPdx structure (*10*), the largest differences between Pdx and Adx are observed in the region of the polypeptide immediately to the N-terminal end of the metal binding loop, residues 32−38 in Pdx. Sequence homology between the two proteins is lowest in this region, and in Pdx, there is a turn-like feature involving residues 32−35, while the same region in Adx is more extended. This difference is likely due to the difference in the sequence positions of Tyr 33 (Pdx) and Phe 43 (Adx). The aromatic rings of the two residues occupy essentially identical positions in their respective structures. However, their backbone positions are not homologous, and different polypeptide conformations appear to be required in order to reach the correct set of folded contacts (Figure 8). The other region where differences are observed is helix **F**, which contributes the side chain of Phe 56 to the major hydrophobic core of Pdx. There is no aromatic residue in Adx that is positionally homologous to Phe 56. Rather, there are two

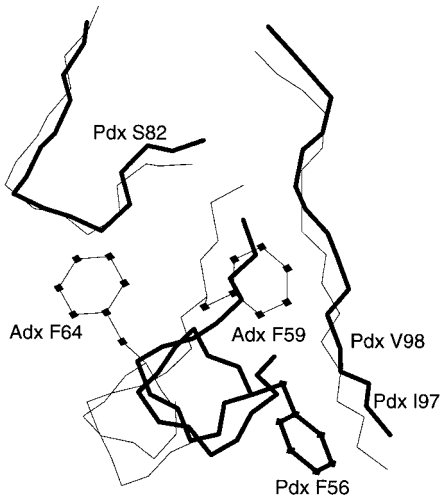

FIGURE 9: Positions of aromatic residues on the **F** helix in Pdx and in Adx. Phe 56 in Pdx abuts strand L, as shown by ring current shifts to Ile 97 and Val 98. The positions of the two aromatic residues in Adx (Phe 59 and Phe 64) shift the helix backbone relative to Pdx. Heavy lines indicate the backbone of Pdx. The backbone of Adx is shown as light lines. The figure was generated using MOLMOL (ETH Zürich).

other aromatic residues on the corresponding helix in Adx, Phe 59, and Phe 64 that displace the helix relative to its position in Pdx (Figure 9).

CONCLUSIONS

The determination of solution structures for Fe_2S_2 ferredoxins by NMR methods is problematic in that paramagnetism renders most standard high-resolution NMR experiments useless near the metal cluster. Although we and others are currently using isotopic labeling to observe and identify resonances in the metal binding loop of Pdx (*49*, *50*), hybrid methods combining experimental and homology data must still be used for generating solution structures for this class of protein (*5*, *50*−*52*). The best test for the usefulness of such hybrid models is an after-the-fact crystal structure of the protein to determine the accuracy of the model. Although we are still analyzing crystallographic data obtained for Pdx, the observed high degree of homology between the positioning of the metal clusters in Pdx and Adx (*11*) justifies the conservative use of homology modeling in these cases. In addition, the supplemental structural restraints provided by NOEs observed in the diamagnetic GaPdx have improved the precision of the model in regions of the structure adjacent to the metal binding site. The generality of gallium reconstitution of this class of proteins (whether as a gallium rubredoxin as with Pdx and Tdx, or as a complete Ga_2S_2 cluster, as has been observed for the plant ferredoxins) provides an important tool for future structural work in this class of protein.

ACKNOWLEDGMENT

The authors thank Dr. Jürgen Müller of the Max Delbruck Institute (Berlin) for access to the coordinates of the bovine adrenodoxin crystal structure.

SUPPORTING INFORMATION AVAILABLE

The complete set of stereospecific ^1H, ^{13}C, and ^{15}N assignments for Pdx^o have been deposited with the BioMagResBank, Madison WI (Accession no. 4154). This material is available free of charge via the Internet at http://pubs.acs.org.

REFERENCES

1. Cushman, D. W., Tsai, R. L., and Gunsalus, I. C. (1967) *Biochem. Biophys. Res. Commun. 26*, 577−583.
2. Lipscomb, J. D., Sligar, S. G., Namtvedt, M. J., and Gunsalus, I. C. (1976) *J. Biol. Chem. 251*, 1116−1124.
3. Stayton, P. S., Poulos, T. L., and Sligar, S. G. (1989) *Biochemistry 28*, 8201−8205.
4. Roitberg, A. E., Holden, M. J., Mayhew, M. P., Kurnikov, I. V., Beratan, D. N., and Vilker, V. L. (1998) *J. Am. Chem. Soc. 120*, 8927−8932.
5. Pochapsky, T. C., Ye, X. M., Ratnaswamy, G., and Lyons, T. A. (1994) *Biochemistry 33*, 6424−6432.
6. Ye, X. M., Pochapsky, T. C., and Pochapsky, S. S. (1992) *Biochemistry 31*, 1961−1968.
7. Rypniewski, W. R., Breiter, D. R., Benning, M. M., Wesenberg, G., Oh, B.-H., Markley, J. L., Rayment, I., and Holden, H. M. (1991) *Biochemistry 30*, 4126−4131.
8. Kazanis, S., Pochapsky, T. C., Barnhart, T. M., Penner-Hahn, J. E., Mirza, U. A., and Chait, B. T. (1995) *J. Am. Chem. Soc. 117*, 337−346.
9. Kazanis, S., and Pochapsky, T. C. (1997) *J. Biomol. NMR 9*, 337−346.
10. Pochapsky, T. C., Kuti, M., and Kazanis, S. (1998) *J. Biomol. NMR 12*, 407−415.
11. Müller, A., Müller, J. J., Muller, Y. A., Uhlmann, H., Bernhardt, R., and Heinemann, U. (1998) *Structure 6*, 269−280.
12. Lyons, T. A., Ratnaswamy, G., and Pochapsky, T. C. (1996) *Protein Sci. 5*, 627−639.
13. Neri, D., Otting, G., and Wuthrich, K. (1990) *Tetrahedron 46*, 3287−3296.
14. Bax, A., and Subramanian, S. (1986) *J. Magn. Reson. 67*, 565−569.
15. Shaka, A. J., Barker, P. B., and Freeman, R. (1985) *J. Magn. Reson. 52*, 335−338.
16. Shaka, A. J., Keeler, J., Frenkiel, T., and Freeman, R. (1983) *J. Magn. Reson. 64*, 335−338.
17. Grzesiek, S., and Bax, A. (1992) *J. Magn. Reson. 96*, 432−440.
18. Kay, L. E., Xu, G. Y., and Yamazaki, T. (1994) *J. Magn. Reson., Ser. A 109*, 129−133.
19. Vuister, G. W., and Bax, A. (1992) *J. Magn. Reson. 98*, 428−433.
20. Bax, A., Clore, G. M., and Gronenborn, A. (1990) *J. Magn. Reson. 88*, 425−431.
21. Shaka, A. J., Lee, C. J., and Pines, A. (1988) *J. Magn. Reson. 77*, 547−552.
22. Bodenhausen, G., and Reuben, D. J. (1980) *Chem. Phys. Lett. 69*, 185−188.
23. Piotto, M., Saudek, V., and Sklenar, V. (1992) *J. Biomol. NMR 2*, 661−665.
24. Neri, D., Szyperski, T., Otting, G., Senn, H., and Wuthrich, K. (1989) *Biochemistry 28*, 7510−7516.
25. Archer, S. J., Ikura, M., Torchia, D. A., and Bax, A. (1991) *J. Magn. Reson. 95*, 636−641.
26. Neri, D., Otting, G., and Wuthrich, K. (1990) *J. Am. Chem. Soc. 112*, 3663−3665.
27. Grzesiek, S., and Bax, A. (1997) *J. Biomol NMR 9*, 207−211.
28. Nilges, M., Clore, G. M., and Gronenborn, A. (1988) *FEBS Lett. 239*, 317−324.
29. Mayerle, J. J., Denmark, S. E., DePamphilis, B. V., Ibers, J. A., and Holm, R. H. (1975) *J. Am. Chem. Soc. 97*, 1032−1045.
30. Laskowski, R. A., Rullmann, J. A., MacArthur, M. W., Kaptein, R., and Thornton, J. M. (1996) *J. Biomol. NMR 8*, 477−486.

31. Beckert, V., Schrauber, H., Bernardt, R., Van Dijk, A. A., Kakoschke, C., and Wray, V. (1995) *Eur. J. Biochem. 231*, 226−235.
32. Uhlmann, H., and Bernhardt, R. (1995) *J. Biol. Chem. 272*, 4883−4888.
33. Burova, T. V., Beckert, V., Uhlmann, H., Ristau, O., Bernhardt, R., and Pfeil, W. (1996) *Protein Sci. 5*, 1890−1897.
34. Holden, M., Mayhew, M., Bunk, D., Roitberg, A., and Vilker, V. (1997) *J. Biol. Chem. 272*, 21720−21725.
35. Aoki, M., Ishimori, K., Morishima, A., and Wada, Y. (1998) *Inorg. Chim. Acta 272*, 80−88.
36. Pochapsky, T. C., Lyons, T. A., Kazanis, S., Arakaki, T., and Ratnaswamy, G. (1996) *Biochimie 78*, 723−733.
37. Vidakovic, M., and Germanas, J. P. (1996) *Protein Sci. 5*, 1793−1799.
38. Unno, M., Christian, J. F., Benson, D. E., Gerber, N. C., Sligar, S. G., and Champion, P. M. (1997) *J. Am. Chem. Soc. 119*, 6614−6620.
39. Reipa, V., Mayhew, M. P., and Vilker, V. L. (1997) *Proc. Natl. Acad. Sci. U.S.A. 94*, 13554−13558.
40. Roitberg, A. E. (1997) *Biophys. J. 73*, 2138−2148.
41. Vo, E., Wang, H. C., and Germanas, J. P. (1997) *J. Am. Chem. Soc. 119*, 1934−1940.
42. Pochapsky, T. C., Ratnaswamy, G., and Patera, A. (1994) *Biochemistry 33*, 6433−6441.
43. Geren, L. M., Tuls, J., O'Brien, P., Millett, F., and Peterson, J. A. (1986) *J. Biol. Chem. 261*, 15491−15495.
44. Sligar, S. G., Debrunner, P. G., Lipscomb, J. D., Namtvedt, M. J., and Gunsalus, I. C. (1974) *Proc. Natl. Acad. Sci. U.S.A. 71*, 3906−3910.
45. Davies, M. D., and Sligar, S. G. (1992) *Biochemistry 31*, 11383−11389.
46. Orme-Johnson, N. R., Mims, W. B., Orme-Johnson, W. H., Bartsch, R. G., Cusanovich, M. A., and Peisach, J. (1983) *Biochim. Biophys. Acta 748*, 68−72.
47. Xia, B., Volkman, B. F., and Markley, J. L. (1998) *Biochemistry 37*, 3965−3973.
48. Pochapsky, T. C., Arakaki, T., Jain, N., Kazanis, S., Lyons, T. A., Mo, H. Ratnaswamy, G., and Ye, X. (1998) *J. Biomol. Struct. Dyn. 16*, 79−89.
49. Jain, N. U., and Pochapsky, T. C. (1998) *J. Am. Chem. Soc. 120*, 12984−12985.
50. Coxon, B., Sari, N., Holden, M. J., and Vilker, V. L. (1997) *Magn. Reson. Chem. 35*, 743−751.
51. Baumann, B., Sticht, H., Scharpf, M., Sutter, M., Haehnel, W., and Rosch, P. (1996) *Biochemistry 35*, 12831−12841.
52. Hatanaka, H., Tanimura, R., Katoh, S., and Inagaki, F. (1997) *J. Mol. Biol. 268*, 922−933.
53. Lelong, C., Setif, P., Bottin, H., Andre, F., and Neumann, J.-M. (1995) *Biochemistry 34*, 14462−14473.
54. Kraulis, P. J. (1991) *J. Appl. Crystallogr. 24*, 946−950.

BI983030B